Three-Dimensional Spatiotemporal Wind Field Reconstruction Based on Physics-Informed Deep Learning

Jincheng Zhang[a], Xiaowei Zhao[a,*]

[a]*Intelligent Control & Smart Energy (ICSE) Research Group, School of Engineering, University of Warwick, Coventry, UK*

Abstract

In this work, a physics-informed deep learning model is developed to achieve the reconstruction of the three-dimensional (3-D) spatiotemporal wind field in front of a wind turbine, by combining the 3-D Navier-Stokes equations and the scanning LIDAR measurements. To the best of the authors' knowledge, this is for the first time that the full 3-D spatiotemporal wind field reconstruction is achieved based on real-time measurements and flow physics. The proposed method is evaluated using high-fidelity large eddy simulations. The results show that the wind vector field in the whole 3-D domain is predicted very accurately based on only scalar line-of-sight LIDAR measurements at sparse locations. Specifically, at the baseline case, the prediction errors for the streamwise, spanwise and vertical velocity fields are $0.263m/s$, $0.397m/s$ and $0.361m/s$, respectively. The prediction errors for the horizontal and vertical direction fields are $2.84°$ and $2.58°$ which are important in tackling yaw misalignment and turbine tilt control, respectively. Further analysis shows that the 3-D wind features are captured clearly, including the evolutions of flow structures, the wind shear in vertical direction, the blade-level speed variations due to turbine rotation, and the speed variations modulated by the turbulent wind. Also, the developed model achieves short-term wind forecasting without the commonly-used Taylor's frozen turbulence hypothesis. Furthermore it is very useful in advancing other wind energy research fields e.g. wind turbine control & monitoring, power forecasting, and resource assessments because the 3-D spatiotemporal information is important for them but not available with current sensor and prediction technologies.

Keywords: Computational fluid dynamics, Light detection and ranging (LIDAR), Navier-Stokes equations, Physics-informed deep learning, Wind field prediction

1. Introduction

As one of the largest sustainable energy resources, wind energy is under intense investment worldwide. It plays a more and more important role in achieving carbon neutrality while meeting the global power demand. However, the spatial and temporal variability of the intermittent and chaotic wind still poses great challenges for wind industry, in the scenarios such as the control design for wind turbines [1, 2], the integration of wind power into the power grid [3, 4], and the wind resource assessment [5, 6]. To tackle these challenges, the accurate prediction of detailed spatiotemporal wind velocity field is of vital importance.

In recent years various measurement technologies, such as wind turbine-mounted light detection and ranging (LIDAR) devices [7], have been used on wind turbines to measure the incoming wind speed. The LIDAR measurement data can be analyzed [8, 9] to provide preview wind information. Meanwhile numerous wind prediction approaches have been proposed and recent advancements include the deep learning ensemble model with data denoising [10], the recurrent neural networks based approach with error correction [11], and the

variational Bayesian deep learning based approach [12]. These studies showed very promising results in wind speed predictions. However, as the wind measurement data is normally only available at sparse spatial locations, the whole flow field in front of the wind turbines remains unknown. Numerical approaches have been investigated to obtain the detailed spatiotemporal wind field information [13, 6], by numerically solving the Navier-Stokes (NS) equations. The integration of wind measurements and numerical simulations has also been explored recently [14]. However, numerical models were mainly designed for forward simulations thus cannot take real-time wind measurements into account. In order to achieve more accurate and more detailed spatiotemporal wind predictions, a very promising direction is to develop a method that can take advantage of both the real-time measurements and the flow physics, therefore achieving superior prediction performance.

Currently, the studies on wind predictions via the fusion of measurement data with flow physics are still rare. In [15], a wind field reconstruction method was proposed by combining a low-order dynamic wind model with LIDAR measurements where an unscented Kalman filter (UKF) was used for state estimations. In [16], to avoid the use of low-order wind models, a spatiotemporal wind prediction framework was proposed where a reduced-order nonlinear model was derived directly from NS equations and then a modified UKF algorithm

---

was employed for state estimations. In [17], a wind field reconstruction method was developed based on computational fluid dynamics (CFD) and proper orthogonal decomposition (POD), where CFD simulations were carried out to generate a database of wind fields and POD was employed to extract the low-dimensional basis vectors. The flow field reconstruction was then carried out through these basis vectors based on measurements from the optimally-placed sensors. The authors of [17] further investigated the optimal design of the sensor arrangement in order to improve the reconstruction performance [18]. To summarize, all these studies showed very promising results, by taking flow physics into account in the wind field reconstruction process (either through dynamic wind model, NS equations or CFD simulations). However, due to the complexity (e.g. the strong nonlinearity and the multi-scale characteristics) of the wind dynamics, the aforementioned studies all included an explicit model reduction process in reconstructing the flow field (i.e. low-order wind model [15], reduced-order model from NS equations [16], dimension reduction by POD [17, 18]). Thus their prediction performances were limited by the explicit model reduction errors. To address these, in our recent study [19], a 2-D spatiotemporal wind field reconstruction was achieved based on NS equations without model reductions, which followed the physics-informed deep learning technique [20] where the 2-D NS equations were incorporated in the deep neural network (NN) structure. However, similarly to the above studies, our work [19] only investigated the reconstructions of the two-dimensional (2-D) flow field, while in practice the wind field is three-dimensional (3-D) and the variation of wind speed in vertical direction (e.g. the wind shear) has a clear impact on the wind turbine loading (in particularly its spatial variations), wind power generations and wind resource assessment [21, 22]. Thus a big research gap still exists.

In order to fill the gap, the present work extends our research in [19] to develop a 3-D spatiotemporal wind field reconstruction method, through combining the 3-D NS equations and the scanning LIDAR measurements into physics-informed deep learning. In particular, a deep NN is first constructed, then the 3-D NS equations are encoded into the deep NN to form the NS residue terms, by using automatic differentiation. Next, the measurement process of the scanning LIDAR is encoded into the deep NN to map the full flow state and the real-time LIDAR beam directions to LIDAR observations. The NN training is finally carried out to minimize the LIDAR observation errors and the NS residues simultaneously. Because the 3-D NS equations can describe the 3D unsteady wind very well (without relying on any reduced-order models or dimension reductions such as POD) while the scanning LIDAR provides sparse yet valuable information about the incoming 3-D wind, the whole 3-D spatiotemporal wind field can be predicted after training. To the best of the authors' knowledge, this is for the first time that the prediction of 3-D spatiotemporal wind field is achieved based on real-time scattered measurements and physics. From the predicted spatiotemporal flow field, the mean wind quantities (such as the effective wind speed at different heights) and the instantaneous wind quantities (such as the wind speed at specific turbine blade locations) can be extracted.

In addition, the present work further improves the wind field reconstruction performance by taking full advantage of the physics-informed deep learning framework's ability in solving inverse problems. In particular, instead of incorporating the NS equations with pre-determined parameters (i.e. the air viscosity in the transport terms), as was done in [19], the present work treats the parameters in the NS equations (i.e. the effective viscosity which is the sum of the air viscosity and turbulent viscosity) as training variables. Therefore, this work achieves the inference of the turbulent viscosity and the reconstruction of the 3-D wind field simultaneously. The benefits of solving the inverse problem instead of directly specifying the NS equations with the air viscosity are two-fold. First, the accuracy of reconstructing the 3-D wind field is improved, as in this way the turbulence effects are taken into account. Second, the turbulent viscosity is obtained after training, which can be used for characterizing the turbulence intensity in other applications such as the modeling and numerical simulation of turbulent wind.

To evaluate the performance of the proposed method, a large-scale CFD flow solver SOWFA (Simulator for Onshore/Offshore Wind Farm Applications) developed by National Renewable Energy Laboratory [23], is employed to carry out high-fidelity numerical experiments for a set of wind speed cases ranging from below-rated, rated, to above-rated conditions of typical wind turbines. SOWFA can simulate the atmospheric boundary layer flows under various conditions and has been widely validated in many studies e.g. on the turbine dynamics [24], the control of wind farms [25, 26] and the wind turbine load in atmospheric flows [27]. During SOWFA simulations, the line-of-sight scalar wind speed at specific spatial locations are extracted to simulate the measurement process of the scanning LIDAR beams, while the 3-D flow fields are recorded to provide ground truth for method validations. The prediction results show that the proposed method can reconstruct the 3-D spatiotemporal wind field (including both wind magnitude and direction) in front of the wind turbine very accurately based on only the scalar LIDAR measurements at sparse spatial locations. In addition, as the deep learning model learns both the spatial and temporal correlations of the evolving wind from NS equations, a short-term wind forecasting without the commonly-used Taylor's frozen turbulence hypothesis [28] is also achieved.

The main contributions and novelties of this paper are summarized as follows:

(1) **The prediction of 3-D spatiotemporal wind field in front of a wind turbine is achieved for the first time, by combing 3-D NS equations and scanning LIDAR measurements via physics-informed deep learning.** In particular, the whole 3-D dynamic wind vector field is reconstructed using only the line-of-sight LIDAR measurements at sparse spatial locations. Because LIDAR devices are becoming widely available for modern wind turbines, and, to the best of the authors' knowledge, no other works can achieve similar 3-D wind predictions, this work is very useful in advancing other research fields including wind turbine control & monitoring, wind resource assessment, and wind power

2

Ref.	Method	Explicit model reduction	Spatial feature	Temporal feature
[15]	low-order wind model + UKF	required	2-D	dynamic
[17, 18]	POD + CFD	required	2-D	static
[16]	2-D NS + UKF	required	2-D	dynamic
[19]	2-D NS + deep learning	not required	2-D	dynamic
this work	3-D NS + turbulent viscosity + deep learning	not required	3-D	dynamic

Table 1: The advantages of the wind field reconstruction method proposed in this work compared with existing works in the literature.

& load forecasting. The advantages of the wind field reconstruction method proposed in this work compared with existing works in the literature are summarized in Table 1. We mention that other machine learning based wind prediction works are not included in this table as they usually can only discover wind information that is present in the training data, while the objective of this paper is to discover the detailed wind information that is not captured in the training data, via the fusion of physics and "small" data.

(2) **Instead of using pre-determined parameters for the NS equations [19], the proposed method treats the unknown parameters (i.e. the turbulent viscosity) in the NS equations as training variables.** In this way, the inference of the turbulent viscosity is achieved which is very useful for other wind applications such as wind modeling and simulations. It also further improves the performance of wind field reconstruction, as the turbulence effects have been taken into account through the turbulent viscosity.

(3) **The proposed method is validated using large-scale high-fidelity numerical experiments for a set of wind speed cases ranging from below-rated, rated, to above-rated conditions of typical wind turbines.** The results show that the 3-D wind vector (including the streamwise, spanwise and vertical velocity) field is predicted accurately for all the cases. In particular, the wind directions in the horizontal plane and vertical plane are both predicted accurately, which is not trivial as only scalar LIDAR measurements are used for the predictions. This demonstrates that the proposed method can be applied to tackle yaw misalignment and turbine tilt control simultaneously.

(4) **The developed method can i) infer the turbulent viscosity; ii) accurately capture the propagation and evolution of the 3-D flow structures, i.e. the high/low speed zones; iii) accurately predict the vertical wind shear, which is of great importance for various wind applications [21, 22]; iv) accurately predict the undisturbed wind speed at specific turbine blade locations, including the wind speed variation due to both turbine rotations and spatially evolving turbulence.** This detailed blade-level wind prediction shows the great potential of the proposed method in assessing turbine blade load and its spatial variations, and in smart rotor design/control [29].

The remaining part of this paper is organized as follows: the spatiotemporal wind field reconstruction problem is formulated in Section 2. The physics-informed deep learning based method which combines the 3-D NS equations and the LIDAR measurements is described in Section 3, where the deep NN structure and its training are given in detail. The prediction performance of the developed method is evaluated in Section 4, using high-fidelity large eddy simulations. Finally the conclusions are drawn in Section 5.

2. Problem Formulation

Currently, LIDAR devices are becoming widely available for modern wind turbines. However, LIDAR can only measure the line-of-sight (LoS) wind speed in the laser beam direction at sparse spatial locations along the laser beams. As the incoming wind in real-world condition is not uniform, the whole 3-D wind field in front of wind turbines remains unknown. In order to bridge the gap between the limitation of the current sensor technology and the need of detailed wind field information, this work develops a method to achieve the reconstruction of the whole 3-D spatiotemporal wind field in front of a wind turbine, based on LIDAR measurements and 3-D NS equations.

An illustration of LIDAR measurements is given in Figure 1, where the LIDAR beams (colored in red) are shown in front of a wind turbine. At a given time instant, the LIDAR beams can measure the LoS wind speed at the discrete spatial locations (which are illustrated as the cross signs in Figure 1). The 3-D spatiotemporal wind field reconstruction problem considered in this work states as, based on the LIDAR measurements at these sparse locations during certain time period T, how to predict the wind velocity (including the wind velocity components in downwind, crosswind, and vertical directions) at every location in the 3-D spatial domain in front of the wind turbine at every time instant. We mention that this task is not achievable without taking flow physics into account, as only scalar measurements (i.e. the LoS wind speed) at sparse locations are available.
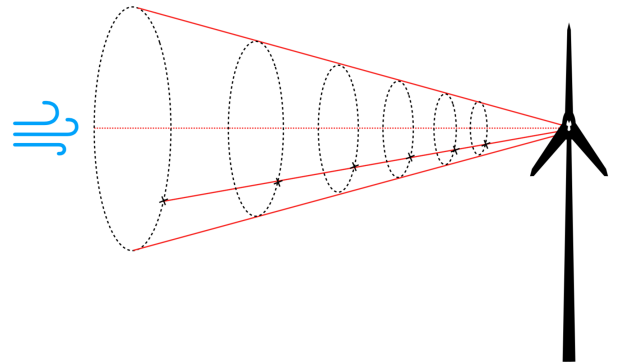

Figure 1: The illustration of LIDAR measurements in front of a wind turbine.

3. 3-D spatiotemporal wind field reconstruction method

A 3-D spatiotemporal wind field reconstruction method is proposed in this section, where LIDAR measurements and 3-D NS equations are combined via the physics-informed deep learning technique. The whole reconstruction framework is demonstrated in Figure 2. The NN structure and its training are described in detail in the rest part of this section.

3.1. Neural network structure

The whole NN structure includes three sub NNs i.e. the Base-NN, the LIDAR-NN and the NS-NN, as shown in Figure 2. The Base-NN is first constructed, based on which the LIDAR-NN and the NS-NN are then derived to incorporate LIDAR measurements and NS equations respectively.

The Base-NN is constructed to approximate the mapping between the spatiotemporal coordinates and the flow state variables. Denote the spatiotemporal coordinates as $X = [t, x, y, z]$ (representing the time coordinate and the space coordinate in the 3-D Cartesian coordinate system) and the flow state variables as $Y = [u, v, w, p]$ (representing the velocity components in the x, y, z directions and the air pressure, respectively), then the Base-NN, denoted as F, can be expressed as

$$Y = F(X; W) \tag{1}$$

where W represents all the training variables in the Base-NN.

As the LIDAR can only measure the LoS wind speed in the LIDAR beam direction, no training target of Y is available. The LIDAR-NN, denoted as F_μ, is constructed to incorporate the LIDAR measurements. As the mapping between the flow state variables to the LoS LIDAR measurements depends on the direction of the LIDAR beam (which depends on the LIDAR configurations and can also change with time in the case of the scanning LIDAR), the LIDAR-NN takes two additional NN inputs i.e. the elevation angle θ and the azimuth angle ϕ of the LIDAR beam. Denote the NN input of F_μ as $X_\mu = [X, \theta, \phi]$. Denote the NN output of F_μ as $Y_\mu = [u_{los}]$ which represents the projection of the wind velocity vector in the LIDAR beam direction. Then the LIDAR-NN can be expressed as

$$
\begin{aligned}
Y_\mu =\, & F_\mu(X_\mu; W) \\
=\, & F(X; W)[1]cos(\theta) - F(X; W)[2]sin(\theta)sin(\phi) \\
& - F(X; W)[3]sin(\theta)cos(\phi).
\end{aligned} \tag{2}
$$

As LIDAR only measures the wind information at sparse locations, the whole 3-D dynamic flow field in front of the wind turbine remains unknown. Here the NS-NN, denoted as F_{ns}, is derived based on the Base-NN to incorporate the NS equations which provide a very good description of the wind dynamics. The derivation is based on the physics-informed deep learning framework, a novel framework for solving forward and inverse problems involving nonlinear PDEs. The applications of physics-informed deep learning in various research domains have seen great successes recently such as in the study of vortex-induced vibrations [30], the discovery of hidden physics from flow visualizations [31] and the analysis of blood flows

[32], which demonstrates the great advantage of combining physics (in terms of PDEs) and data in various scenarios. In this work, for the wind field reconstruction, the 3-D NS equations

$$\frac{\partial u}{\partial t} + u\frac{\partial u}{\partial x} + v\frac{\partial u}{\partial y} + w\frac{\partial u}{\partial z} = -\frac{\partial p}{\partial x} + \frac{1}{Re}(\frac{\partial^2 u}{\partial x^2} + \frac{\partial^2 u}{\partial y^2} + \frac{\partial^2 u}{\partial z^2})$$

$$\frac{\partial v}{\partial t} + u\frac{\partial v}{\partial x} + v\frac{\partial v}{\partial y} + w\frac{\partial v}{\partial z} = -\frac{\partial p}{\partial y} + \frac{1}{Re}(\frac{\partial^2 v}{\partial x^2} + \frac{\partial^2 v}{\partial y^2} + \frac{\partial^2 v}{\partial z^2})$$

$$\frac{\partial w}{\partial t} + u\frac{\partial w}{\partial x} + v\frac{\partial w}{\partial y} + w\frac{\partial w}{\partial z} = -\frac{\partial p}{\partial z} + \frac{1}{Re}(\frac{\partial^2 w}{\partial x^2} + \frac{\partial^2 w}{\partial y^2} + \frac{\partial^2 w}{\partial z^2})$$

$$\frac{\partial u}{\partial x} + \frac{\partial v}{\partial y} + \frac{\partial w}{\partial z} = 0$$

are first reformulated as

$$e_u = \frac{\partial u}{\partial t} + u\frac{\partial u}{\partial x} + v\frac{\partial u}{\partial y} + w\frac{\partial u}{\partial z} + \frac{\partial p}{\partial x} - \frac{1}{Re}(\frac{\partial^2 u}{\partial x^2} + \frac{\partial^2 u}{\partial y^2} + \frac{\partial^2 u}{\partial z^2})$$

$$e_v = \frac{\partial v}{\partial t} + u\frac{\partial v}{\partial x} + v\frac{\partial v}{\partial y} + w\frac{\partial v}{\partial z} + \frac{\partial p}{\partial y} - \frac{1}{Re}(\frac{\partial^2 v}{\partial x^2} + \frac{\partial^2 v}{\partial y^2} + \frac{\partial^2 v}{\partial z^2})$$

$$e_w = \frac{\partial w}{\partial t} + u\frac{\partial w}{\partial x} + v\frac{\partial w}{\partial y} + w\frac{\partial w}{\partial z} + \frac{\partial p}{\partial z} - \frac{1}{Re}(\frac{\partial^2 w}{\partial x^2} + \frac{\partial^2 w}{\partial y^2} + \frac{\partial^2 w}{\partial z^2})$$

$$e_{div} = \frac{\partial u}{\partial x} + \frac{\partial v}{\partial y} + \frac{\partial w}{\partial z}.$$

Here Re is defined as $U_\infty D/\nu_{eff}$ with D, U_∞, and ν_{eff} representing the turbine rotor diameter, the average freestream wind speed, and the total effective viscosity respectively. The effective viscosity is defined as $\nu_{eff} = \nu_{air} + \nu_t$, where ν_{air} and ν_t are the kinematic viscosity of air and the turbulent viscosity respectively. As the effective viscosity ν_{eff} (thus Re) is not known, it is treated as training variables and is inferred through the training process. The NS equations are then used to form the NS residue terms in the NS-NN. In particular, the differential terms in the NS equations are derived based on the Base-NN using automatic differentiation [33]. For example, to incorporate the term $\partial u/\partial x$ in the NS-NN, the gradient of $F(X; W)[1]$ with respect to $X[2]$, denoted as $\partial F_1(X, W)/\partial X_2$, is derived using automatic differentiation. Other first-order terms are obtained similarly. Then the higher-order terms are obtained by the automatic differentiation of the lower-order terms. For example, to incorporate the term $\partial^2 u/\partial x^2$ in the NS-NN, the gradient of $\partial F_1(X, W)/\partial X_2$ with respect to $X[2]$ is derived. All the terms are finally added to form the NS residue terms $e_u(X; [W, 1/Re])$, $e_v(X; [W, 1/Re])$, $e_w(X; [W, 1/Re])$ and $e_{div}(X; W)$. Denote the NN input and the NN output of F_{ns} as $X_{ns} = [t, x, y, z]$ and $Y_{ns} = [e_u, e_v, e_w, e_{div}]$, the NS-NN can then be expressed as

$$Y_{ns} = F_{ns}(X_{ns}; [W, 1/Re]). \tag{3}$$

As can be seen from the above construction process, the Base-NN, the LIDAR-NN and the NS-NN share the same training variables W. The training of the whole NN involves the updating of W and $1/Re$ to minimize the NN loss function, which will be described in detail in the next subsection.
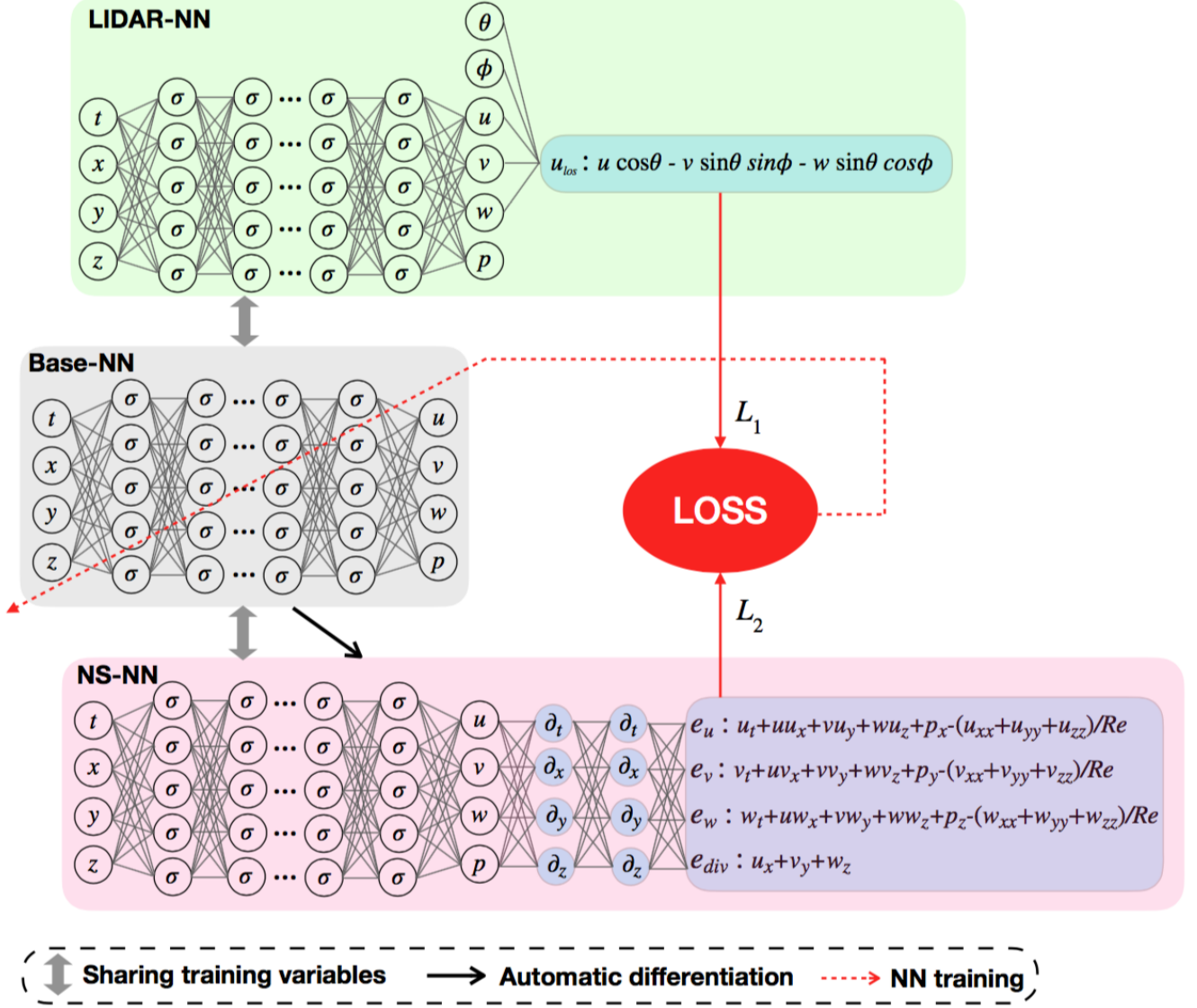
4

Figure 2: The demonstration of the proposed 3-D spatiotemporal wind field reconstruction method based on the physics-informed deep learning technique.

3.2. Neural network training

After constructing the whole NN structure, the loss function needs to be specified for the NN training. In order to train the NN such that it satisfies the constraints imposed by the NS residue terms and fits the LIDAR measurements simultaneously, the loss function is specified to consist of two parts. The first part is defined as

$$L_1(W) = \frac{1}{N_\mu} \sum_{i=1}^{N_\mu} |F_\mu(t_i^\mu, x_i^\mu, y_i^\mu, z_i^\mu, \theta_i^\mu, \phi_i^\mu; W) - u_i^\mu|^2 \quad (4)$$

where $\{[t_i^\mu, x_i^\mu, y_i^\mu, z_i^\mu, \theta_i^\mu, \phi_i^\mu, u_i^\mu], 1 \le i \le N_\mu\}$ are the LIDAR measurement data with each sample consisting of the time coordinate, the measurement location, the elevation angle, the azimuth angle, and the corresponding value of the LoS wind speed

measured by LIDAR. The second part is defined as

$$L_2(W, 1/Re) = \frac{1}{N_{ns}} \sum_{i=1}^{N_{ns}} |F_{ns}(t_i^{ns}, x_i^{ns}, y_i^{ns}, z_i^{ns}; [W, 1/Re])|^2 \quad (5)$$

where $\{[t_i^{ns}, x_i^{ns}, y_i^{ns}, z_i^{ns}], 1 \le i \le N_{ns}\}$ are the randomly-sampled spatiotemporal coordinates corresponding to the spatial domain in front of the wind turbine. It is at these spatiotemporal coordinates that the NS constraints are enforced. The loss function is then defined as

$$L(W, 1/Re) = L_1(W) + L_2(W, 1/Re). \quad (6)$$

Finally, the proposed NN structure is trained to minimize the loss function $L(W, 1/Re)$, by updating the training variables W and $1/Re$. In this work, the Adam algorithm [34] is employed for the NN training.

After the NN training, $1/Re$ (thus the effective viscosity ν_{eff}) can be obtained and the Base-NN can be used for the prediction

of the wind velocity vector at a given location in front of the wind turbine and a given time instant. The whole wind field at a given time instant can thus be obtained by first generating a 3-D mesh corresponding to the flow domain in front of the turbine and then propagating the 3-D mesh through the Base-NN. Furthermore, because the deep learning model learnt the spatiotemporal correlation of the wind field from the NS equations, future time instant can be directly fed into the Base-NN for predictions. Therefore, the proposed method can also achieve a short-term wind forecasting without the commonly-used Taylor's frozen turbulence hypothesis. The detailed training and prediction procedure is summarized in Appendix A.

4. Results

The proposed wind field reconstruction method is evaluated in this section, by using high-fidelity numerical experiments. The simulation details and the prediction results are presented in the following subsections.

4.1. Simulation setups

The numerical experiments are carried out using the high-fidelity large eddy simulation solver SOWFA [23], which has been widely validated and used for simulating atmospheric boundary layer flows and wind farm wake flows [24, 25]. More details regarding the simulation validations and comparisons can be found in [26]. For the simulations in this work, a 3-D mesh of $250 \times 250 \times 83$ is generated in a $3km \times 3km \times 1km$ flow domain, so that the atmospheric boundary layer flows can be captured correctly [24]. The corresponding flow domain is illustrated in Figure 3, where the contour shows the instantaneous wind velocity field. For all the wind conditions considered in this work, simulations of $20000s$ are first carried out with a time step of $0.5s$ in order to establish the quasi-equilibrium flow state which will be used as the initial flow field for the subsequent simulations. Then the simulations of $400s$ with a time step of $0.02s$ are carried out where the whole 3-D wind velocity field (including the wind speed in the x, y, z directions at every spatial location) is recorded during the last $100s$ simulations. The recorded wind field data is not used for training the developed machine learning model and it is only used as the ground truth for method validations. All the simulations are carried out using 256 CPU cores on local high-performance computing clusters and each case requires around 17 hours for the total simulations of $20400s$.

In addition, a virtual LIDAR device is added to extract the LoS wind speed at the LIDAR measurement locations. In particular, five LIDAR beams, with the measurement frequency of 1s, the spatial resolution of 20m and the measurement range of 220m, are included in the virtual measurement process. One of five beams is configured towards the turbine yaw direction i.e. the elevation angle equal to $0°$. The other four are configured with an elevation angle of $15°$ and uniformly-distributed azimuth angles (i.e. the four beams are uniformly distributed in the cone surface as illustrated by the red lines in Figure 1). Furthermore, the virtual LIDAR beams are designed to scan over
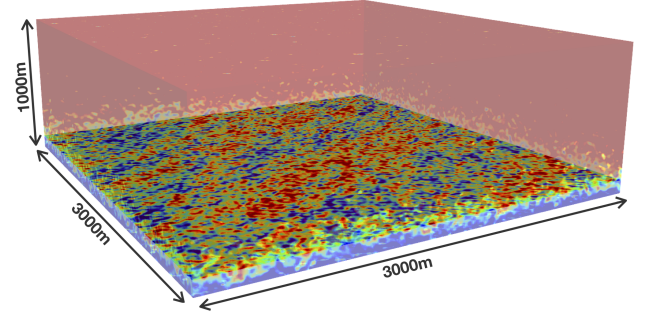

Figure 3: The illustration of the flow domain for the numerical simulations, where the contour shows the instantaneous wind velocity field.

Effective viscosity	Turbulent viscosity ratio
$0.2m^2/s$	2.0×10^4

Table 2: The estimation of the effective viscosity by the proposed method.

the azimuth direction in order to provide the wind information with better spatial coverage.

In the following subsections, the wind field prediction at a baseline case is first investigated, where the freestream wind speed is set as $8m/s$ (which corresponds to a Reynolds number of 4.8×10^7) and the freestream turbulence intensity is set as 6%, then a parametric study is carried out to evaluate the performance of the developed method for a set of wind speeds i.e. $13m/s$, $18m/s$, and $23m/s$.

4.2. Prediction results and discussions

The LIDAR measurement data, which is described in Section 4.1, is used to train the proposed deep learning model. In this work, the structure of the Base-NN is set as 4-128-128-128-128-128-128-128-4 with the hyperbolic tangent activation for the intermediate layers and the linear activation for the last layer. The learning rate of the Adam optimizer is set as 10^{-4}. The training is carried out using NVIDIA Tesla K80 GPU and each training iteration requires around 0.14s, which illustrates the ability of the proposed approach for real-time 3-D dynamic wind field reconstruction through offline training and online updating. The scanning speed of the LIDAR beams in the azimuth direction still needs to be specified. In this work, the scanning speed is determined by trial and error and is set as a constant value of $15°/s$.

After training, the effective viscosity is obtained. The results are given in Table 2, along with the turbulent viscosity ratio i.e. the ratio between the turbulent viscosity and the air viscosity. The results clearly show that the turbulent wind is characterized primarily by the turbulent viscosity, as the effective viscosity is much larger than the air viscosity. As the turbulent viscosity can be used to describe the wind turbulence, it is very useful for other wind applications such as wind modeling and simulations. For example, it can be used to specify the turbulent inflow conditions for numerical simulations of wind turbine wakes.

Next, the whole spatiotemporal 3-D flow field is predicted. The results for three typical time instants are given in Figure 4

and Figure 5, where the corresponding ground truth and error distribution are also included. Figure 4 shows the visualizations of the wind speed magnitude in the x-y plane at the hub height and in the x-z plane, while Figure 5 shows the flow visualizations in the y-z plane at various streamwise locations. As can be seen from Figure 4, the flow structures (e.g. the high-speed/low-speed flow zones) in both x-y and x-z planes are predicted very accurately. The wind features in the vertical direction, such as the wind shear (e.g. the increase of the wind speed with height), are also captured very well. As can be seen from Figure 5, the flow fields in the 2-D domain parallel to the rotor plane are predicted very accurately at various streamwise locations before the turbine. This demonstrates that the proposed method can provide detailed preview wind information for the whole 2-D rotor plane, which is of great importance for the control of wind turbines especially in the case of smart rotors [29]. The error distribution further shows that the prediction errors remain very small for the whole flow domain of interest. The maximum error happens at the locations that are far away from (thus of little importance for) the turbine structures, which is reasonable as no measurements are available in the vicinity of these locations. In addition, the unsteady flow visualizations including both the ground truth and the prediction results are given in the supporting material of this paper (see Video 1 & 2). As shown in the videos, the predicted flow field matches with the ground truth very well, demonstrating that the proposed approach captures the 3-D spatial variation and the temporal evolution of the incoming turbulent wind successfully. The results fully reveal the great performance of the proposed approach.

To further quantify the prediction accuracy, the root mean square error (RMSE) of the flow field prediction is calculated, which is defined as

$$\epsilon_q = \frac{1}{T} \sum_{t=1}^{T} \sqrt{\frac{1}{N_{test}} \sum_{i=1}^{N_{test}} (q^*_{x_i,y_i,z_i,t} - \hat{q}_{x_i,y_i,z_i,t})^2}. \qquad (7)$$

Here the total time T is 100, $\{[x_i, y_i, z_i], 1 \le i \le N_{test}\}$ is the grid points corresponding to the $12m \times 12m \times 12m$ uniform mesh in the 3-D flow domain in front of the wind turbine, and q represents the flow quantity such as the wind velocity components in x, y and z directions (i.e. u, v, w). q^* and $\hat{q}$ represent the true value and the corresponding predicted value of q. The results are given in Table 3. As can be seen, the predictions for the streamwise velocity u, the spanwise velocity v and the vertical velocity w are all quite accurate, with the RMSEs equal to 6.5%, 11.9%, and 12.7% of the corresponding value ranges. Furthermore, the directional information of the wind velocity can also be predicted, by first projecting the 3-D velocity vector to the 2-D plane and then calculating the angle between the 2-D vector and the reference direction. The directions of the wind vector projected in $x - y$ and $x - z$ planes, at any given location, can be calculated by

$$\gamma_y = arctan(v/u) \qquad (8)$$

Case	Quantity	Value range	RMSE (% of range)
8m/s	u (m/s)	[6.08, 10.11]	0.263 (6.5%)
	v (m/s)	[-1.82, 1.53]	0.397 (11.9%)
	w (m/s)	[-1.48, 1.36]	0.361(12.7%)
	γ_y (°)	[-11.4, 11.8]	2.84 (12.2%)
	γ_z (°)	[-10.1, 9.77]	2.58(13.0%)
13m/s	u (m/s)	[9.53, 16.07]	0.592 (9.1%)
	v (m/s)	[-2.89, 2.90]	0.625 (10.8%)
	w (m/s)	[-2.53, 2.56]	0.590 (11.6%)
	γ_y (°)	[-12.6, 12.4]	2.76 (11.0%)
	γ_z (°)	[-10.3, 10.9]	2.60 (12.3%)
18m/s	u (m/s)	[13.14, 21.62]	0.958 (11.3%)
	v (m/s)	[-4.18, 4.47]	0.837 (9.7%)
	w (m/s)	[-4.04, 3.50]	0.774 (10.3%)
	γ_y (°)	[-11.9, 14.9]	2.73 (10.2%)
	γ_z (°)	[-12.1, 12.1]	2.52 (10.4%)
23m/s	u (m/s)	[16.53, 28.44]	1.296 (10.9%)
	v (m/s)	[-4.57, 5.79]	1.098 (10.6%)
	w (m/s)	[-4.82, 5.12]	1.036 (10.4%)
	γ_y (°)	[-11.2, 12.8]	2.72 (11.3%)
	γ_z (°)	[-11.7, 13.1]	2.57 (10.4%)

Table 3: The RMSEs of the flow field predictions for a set of wind speed cases ranging from below-rated, rated, to above-rated conditions of typical wind turbines.

and

$$\gamma_z = arctan(w/u). \qquad (9)$$

The RMSEs of the γ_y and γ_z fields are also included in Table 3. As shown, γ_y, which is actually the conventional wind direction, is predicted correctly. This demonstrates that the proposed approach can be used for tackling the yaw misalignment which is of great importance for improving the efficiency of wind power generations [35]. The vertical wind direction γ_z is also predicted correctly, which shows that the proposed approach can be used for the control of turbine tilt angles [36]. It is concluded that the proposed method predicts the directional wind information very well, given that only scalar information is available in the original LIDAR measurements.

In addition, the 3-D spatiotemporal wind field reconstruction is also carried out by using the pre-determined viscosity in the NS equations. The prediction RMSEs are reported in Appendix B for comparisons with Table 3. The results clearly demonstrate that by including and inferring the effective viscosity in the proposed model, the present work achieves better accuracy for all the flow quantities.
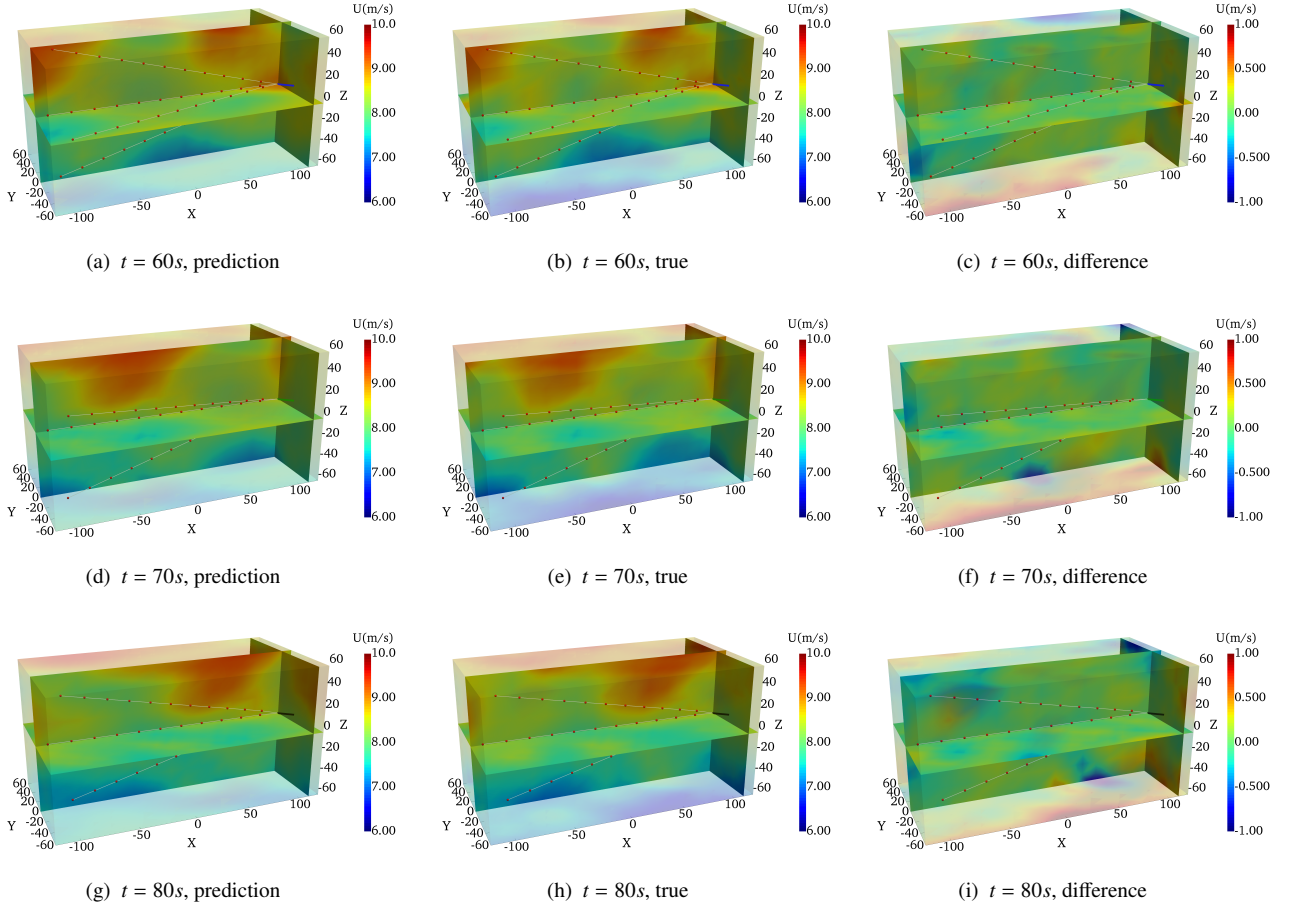
(a) $t = 60s$, prediction   (b) $t = 60s$, true   (c) $t = 60s$, difference

(d) $t = 70s$, prediction   (e) $t = 70s$, true   (f) $t = 70s$, difference

(g) $t = 80s$, prediction   (h) $t = 80s$, true   (i) $t = 80s$, difference

Figure 4: The 3-D velocity field (visualized in x-y and x-z planes) predicted by the proposed method at time (a) $t = 60s$, (d) $t = 70s$ and (g) $t = 80s$. The corresponding ground truth and the difference between prediction and true flow fields are shown in (b, e, h) and (c, f, i), respectively.

To further evaluate the prediction performance and to illustrate the use of the proposed method for wind turbine control and wind power & load forecasting, the 2-D wind field near the LIDAR, the effective wind speed, and the instantaneous wind speed at specific turbine blade locations are extracted from the predicted full spatiotemporal wind field and then compared with the corresponding true values in the following parts.

First, the prediction of the 2-D wind field near the LIDAR (which is located on turbine nacelle) is investigated. The prediction results are given in Table 4. As shown, the prediction RMSEs remain very small for all the main wind quantities including the wind velocity magnitudes and directions. The corresponding unsteady flow visualizations including both the ground truth and the prediction results are given in the supporting material of this paper (see Video 3). As shown in the video, the spatiotemporal wind evolution in this region is predicted very accurately.

Second, the effective wind speed, which is defined here as the wind speed averaged over the y direction, is calculated as

$$\bar{U}_{x_0,t}(z) = \frac{1}{N_y} \sum_{i=1}^{N_y} \hat{u}_{x_0,y_i,z,t}, \quad (10)$$

where $\{y_i, 1 \le i \le N_y\}$ is a set of uniformly-distributed y coordi-

Quantity	Value range	RMSE (% of range)
u (m/s)	[6.88, 9.44]	0.216 (8.4%)
v (m/s)	[-1.57, 1.25]	0.392 (13.9%)
w (m/s)	[-1.29, 1.24]	0.341 (13.5%)
γ_y (°)	[-10.1, 9.89]	2.76 (13.8%)
γ_z (°)	[-9.14, 8.55]	2.43 (13.7%)

Table 4: The RMSEs of the flow field predictions near the LIDAR.

nates in the interval $[-30, 30]m$. We mention that the effective wind speed is defined here as the wind speed averaged only over the y direction instead of over the y-z rotor plane, because in this way the wind speed variation in vertical direction can be shown clearly. The results are given in Figure 6 for several streamwise locations i.e. $x_0 = [-50, -10, 30, 70, 110]m$. As shown, the profiles of the effective wind speed are predicted accurately at all the streamwise locations and all time instants. The wind shear, i.e. the increase of the wind speed magnitude with height, is captured very well.

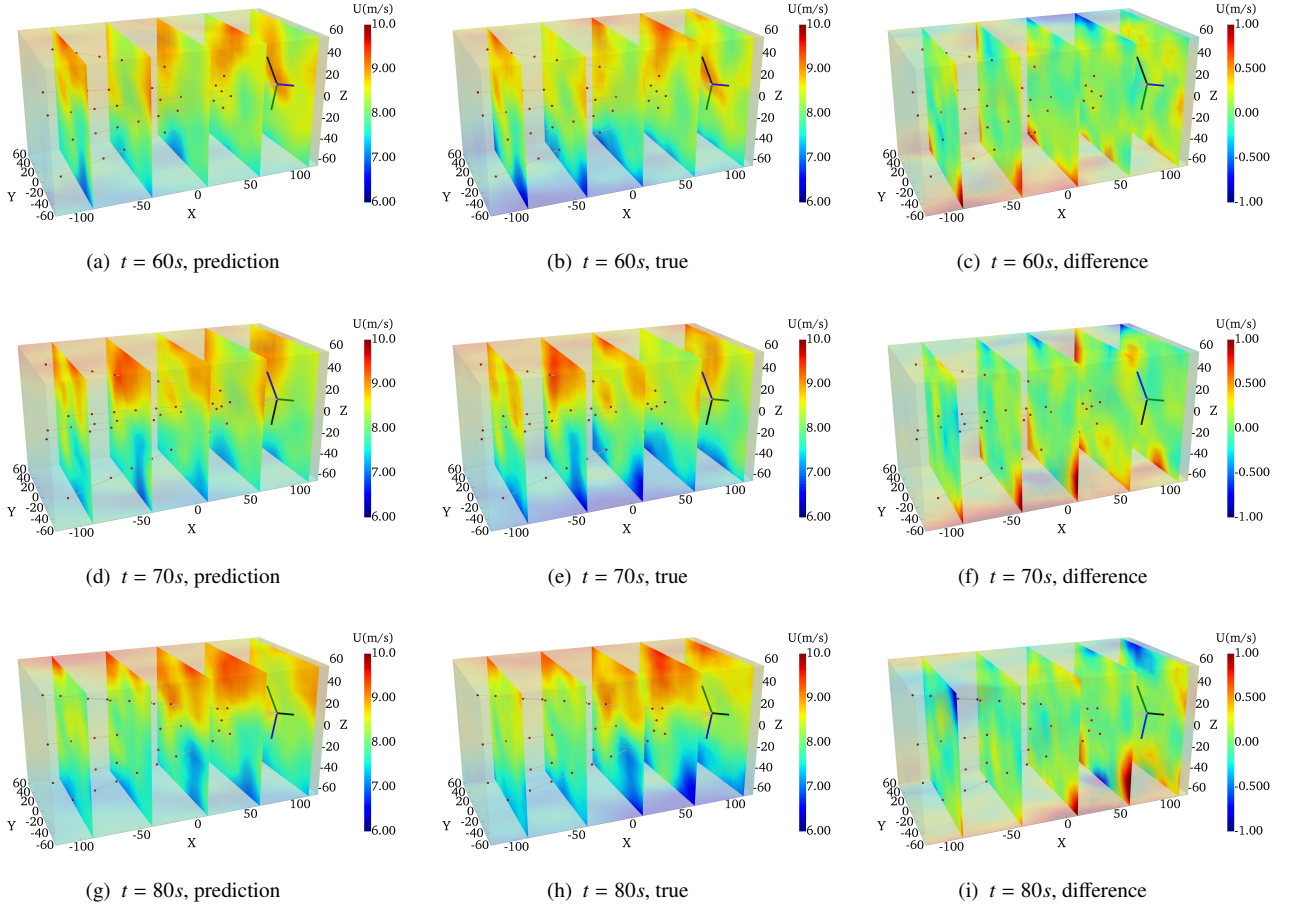Third, the instantaneous wind speeds at the turbine blade

8

(a) $t = 60s$, prediction   (b) $t = 60s$, true   (c) $t = 60s$, difference

(d) $t = 70s$, prediction   (e) $t = 70s$, true   (f) $t = 70s$, difference

(g) $t = 80s$, prediction   (h) $t = 80s$, true   (i) $t = 80s$, difference

Figure 5: The 3-D velocity field (visualized in y-z planes) predicted by the proposed method at time (a) $t = 60s$, (d) $t = 70s$ and (g) $t = 80s$. The corresponding ground truth and the difference between prediction and true flow fields are shown in (b, e, h) and (c, f, i), respectively.

root, 1/4 chord length, 1/2 chord length, 3/4 chord length and the blade tip are predicted and compared with the corresponding ground truth. For illustration purpose, here the rotational speed of the wind turbine is set as $60°/s$, and the variable rotational speed can be applied in the same way. The results are given in Figure 7. As shown, the time series of the wind speed are predicted very accurately, including both the slow variations due to the freestream flow structures and the fast variations due to the turbine rotations. In particular, the effect of the wind shear increases clearly from the blade root to the blade tip location, as shown by the increase of the oscillation magnitudes from Figure 7(a) to 7(e). The magnitudes of wind speed oscillations, which are modulated by the incoming turbulent wind and differ for each turbine rotation period, are also predicted accurately. In addition, the mean values and the standard deviations of the prediction errors during the considered time period are shown in Figure 7(f). As shown, the prediction errors are very small for all the locations. It is also interesting to note that the prediction errors increase slowly from the turbine blade root to the blade tip locations, as the wind speed varies more dramatically from the blade root to tip locations thus making the prediction increasingly difficult from Figure 7(a) to 7(e).

Next, as the proposed deep learning model learns the tem-

poral correlations of the wind field from the NS equations, it can be used directly for short-term wind forecasting. This is achieved by directly feeding future time coordinates to the Base-NN. The results for $15s$-ahead wind speed forecasting are included in Figure 7. Another $15s$ numerical simulations are also carried out by SOWFA to obtain the corresponding ground truth for comparisons. As shown by the last $15s$ time series in Figure 7, the forecasting results match with the true values quite well. We mention that the proposed method does not need any prior parameter tunings to determine the forecasting time horizon. The forecasting can be achieved with good accuracy as long as the wind speed at the location and the time instant of interest is correlated with the available LIDAR measurement data. In practice, the maximum forecasting time horizon can be estimated as the virtual time of the flow convection from the upstream measurement points to the turbine location.

4.3. Sensitivity of prediction accuracy to wind speed

The above results show great accuracy of the proposed wind prediction method at the baseline case. To further validate the proposed method's performance, this subsection is devoted to the 3-D spatiotemporal wind field predictions for a set of wind speed cases, i.e. $13m/s$, $18m/s$, and $23m/s$.
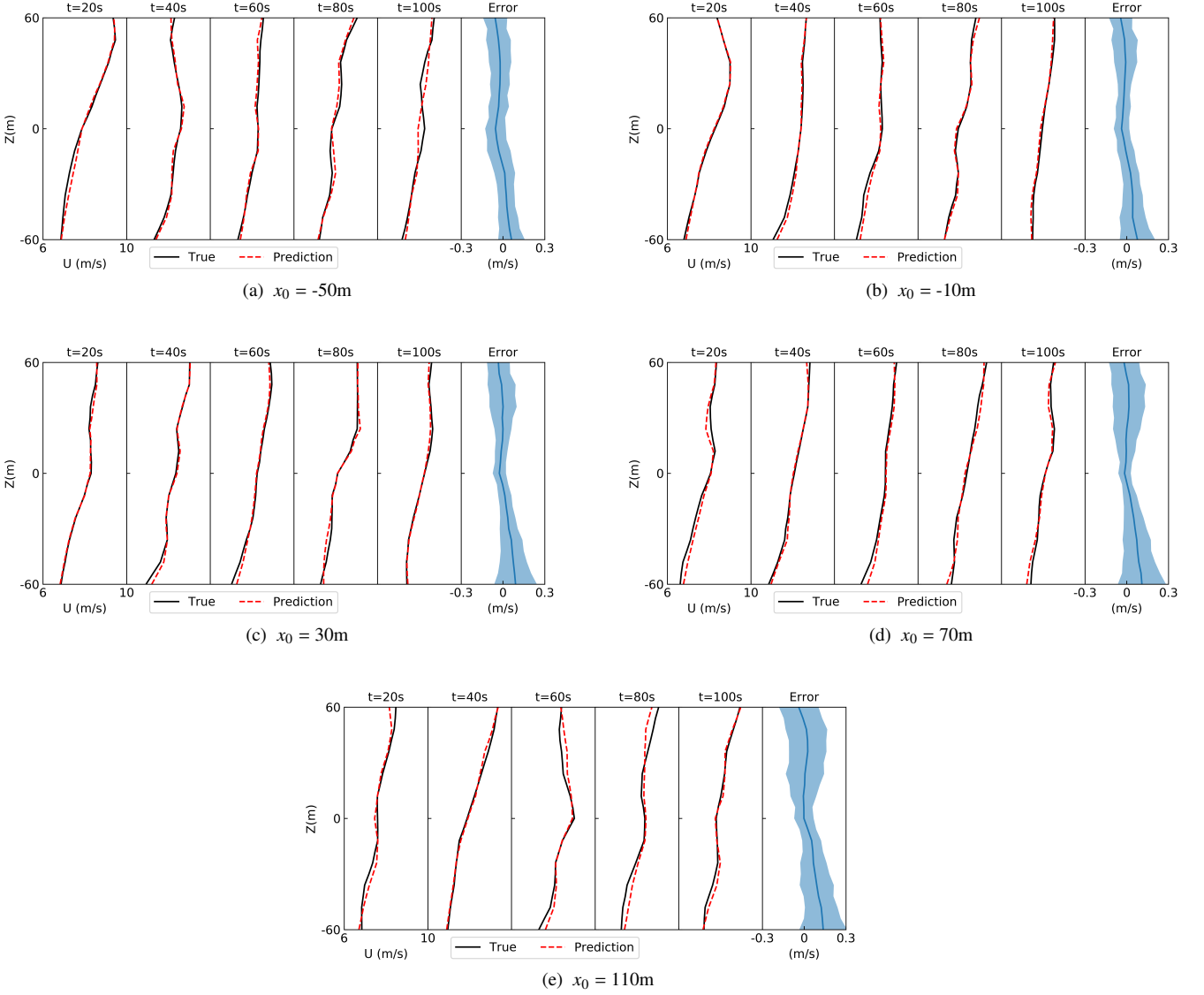
Figure 6: The profile of the effective wind speed predicted by the proposed method (the dashed lines) and the corresponding true values (the solid lines), at $x_0 = [-50, -10, 30, 70, 110]m$ and various time instants. The mean values and the standard deviations of the prediction errors during the considered time period are also shown.

First, the prediction RMSEs are calculated and the results are given in Table 3. As can be seen, for all the cases, the proposed method achieves the accurate prediction of the wind velocity fields for all the flow quantities including both wind magnitudes and directions. Then, the unsteady 3-D flow field visualizations are compared with the corresponding ground truth. The results are given in the supporting material of this paper (see Video 4). Similar to the baseline case, the 3-D spatial variation and the temporal evolution of the turbulent wind are predicted very accurately for all these cases. Also, we mention that all the parameters involved in the model construction and training process are the same as the baseline case, showing that parameter tuning is not needed for different wind speed scenarios. This parametric study thus fully demonstrates the great accuracy and robustness of the proposed method.

5. Conclusions

The 3-D spatiotemporal wind field reconstruction was investigated in this work, where a physics-informed deep learning based method was proposed to combine the 3-D Navier-Stokes equations and the scanning LIDAR measurements. The results showed that, by combing the physics and data, the whole 3-D dynamic wind velocity vector field (including the velocity components in x, y, and z directions) in front of the wind turbine was predicted very accurately based on only the limited scalar information at very sparse spatial locations (i.e. the line-of-sight wind speed measured by LIDAR beams). In addition, the inference of the turbulent viscosity was also achieved, which can be used for characterizing the wind turbulence in other applications such as wind modeling and numerical simulations of

10

(a) blade root (b) 1/4 chord length (c) 1/2 chord length

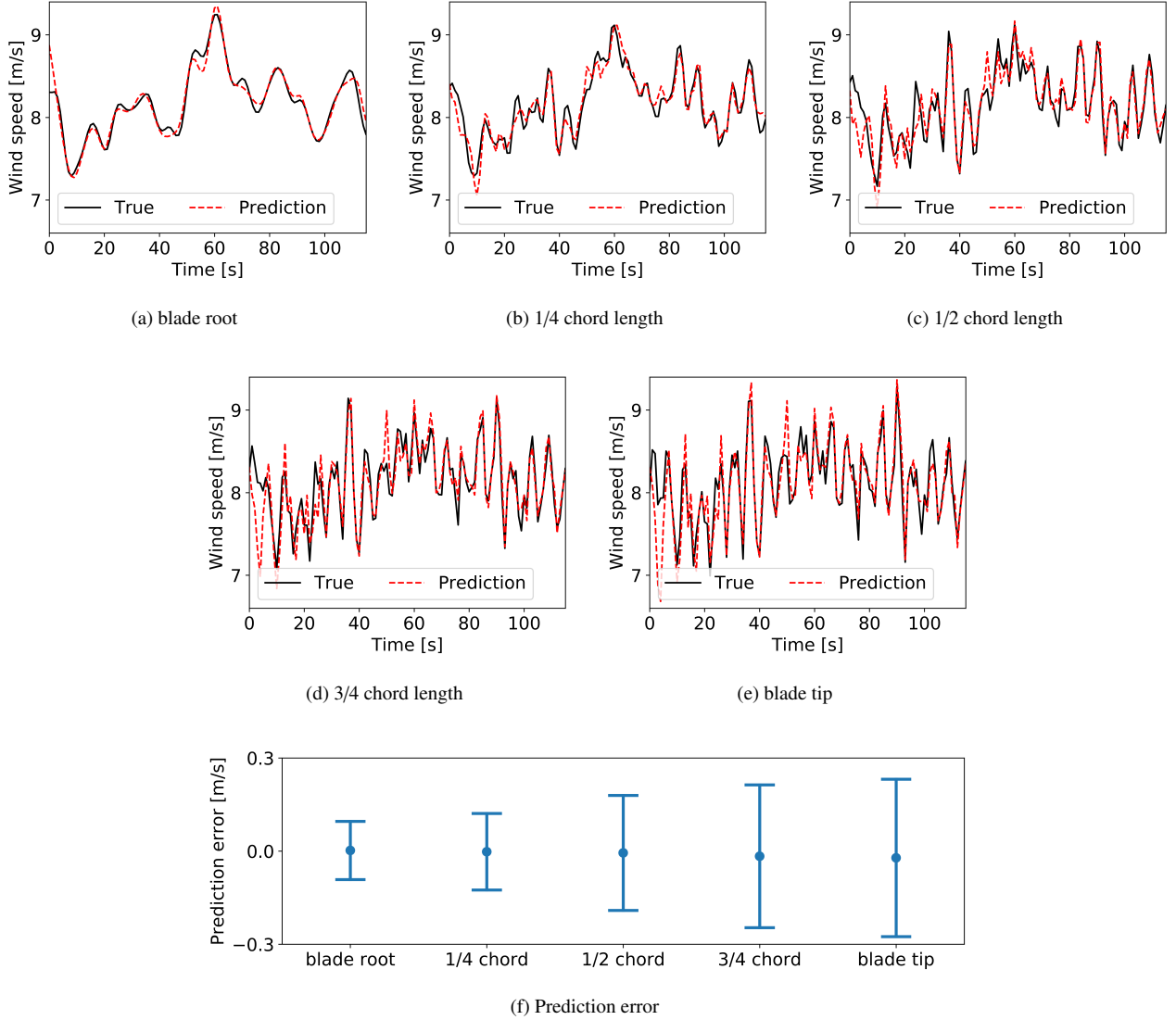(d) 3/4 chord length (e) blade tip

(f) Prediction error

Figure 7: The instantaneous wind speeds predicted by the proposed method (the dashed lines) and the corresponding true values (the solid lines), at (a) the turbine blade root, (b) 1/4 chord length, (c) 1/2 chord length, (d) 3/4 chord length, and (e) the blade tip. Subfigure (f) shows the mean values and the standard deviations of the prediction errors during the considered time period.

wind turbine wakes.

The 3-D wind field predictions were first examined by visualizing the flow fields in x-y, x-z, and y-z planes. The results showed that the spatiotemporal flow field predicted by the proposed approach matched with the corresponding ground truth very well, where the 3-D spatial variation of the incoming wind (such as the evolving flow structures and the vertical wind shear) was successfully predicted. The prediction accuracy was then quantified by the RMSEs of the reconstructed spatiotemporal wind fields. The RMSEs at the baseline case were only $0.263m/s$, $0.397m/s$, $0.361m/s$ for the streamwise velocity u, the spanwise velocity v, and the vertical velocity w, demonstrating the great accuracy of the proposed method. To the best of the authors' knowledge, this is for the first time that this type of accurate and detailed predictions of the unsteady 3-D wind field in front of a wind turbine is achieved. Furthermore, the

directional wind information, including the conventional wind direction (i.e. the wind direction in the $x - y$ plane) and the vertical wind direction (i.e. the wind direction in the $x - z$ plane), was also predicted. The results showed that the RMSEs were only $2.84°$ and $2.58°$ respectively, demonstrating the great potential of the proposed method in tackling yaw misalignment and turbine tilt control, which are of great interest in improving the energy capture efficiency of wind turbines. For example, the field test in [37] showed that the annual energy production could be increased by 2.4% by applying yaw corrections, and the study in [36] showed that turbine tilt control has a great impact on the power generation of wind farms. Furthermore, a parametric study was carried out for a set of wind speed cases ranging from below-rated, rated, to above-rated conditions of typical wind turbines. The results showed that the predicted 3-D spatiotemporal wind field matched well with the corresponding

ground truth for all the cases, demonstrating the great accuracy and robustness of the proposed method.

The predicted wind field is of vital importance for wind energy applications e.g. wind turbine control design to further increase the power generation efficiency, accurate forecasting of wind power to assist its grid integration, and detailed and reliable wind resource assessments. To illustrate these points, the 2-D wind field near the LIDAR, the effective wind speeds at various streamwise locations, and the instantaneous wind speeds at various turbine blade locations were extracted from the predicted wind field and then compared with the corresponding ground truth. The results showed that they were all predicted very accurately. In particular, the wind speed oscillations due to the blade rotations and the variations of the oscillation magnitudes at each rotation period due to the freestream turbulent wind were both captured very well. The vertical wind shear was also predicted accurately. Furthermore, a short-term wind forecasting was carried out and the results showed that the accurate forecasting of the wind speeds at various locations ranging from the turbine blade root to the blade tip was achieved.

To further improve the prediction performance, future works include the design of the LIDAR configuration and its scanning pattern to optimally arrange the measurement points, and the incorporation of other flow sensors in the proposed method to provide more versatile flow measurements.

Acknowledgments

Appendix A. The detailed training and prediction procedure

The detailed training and prediction procedure of the proposed method is summarized below as Algorithm 1.

Appendix B. The prediction results using pre-determined viscosity

The 3-D spatiotemporal wind field prediction at the baseline case is also carried out by using pre-determined parameters (i.e. the air viscosity) in the NS equations. The results are given in Table B.5.

References

Quantity	Value range	RMSE (% of range)
u (m/s)	[6.08, 10.11]	0.276 (6.8%)
v (m/s)	[-1.82, 1.53]	0.457 (13.6%)
w (m/s)	[-1.48, 1.36]	0.364(12.8%)
γ_y (°)	[-11.4, 11.8]	3.25 (14.0%)
γ_z (°)	[-10.1, 9.77]	2.61(13.1%)

Table B.5: The RMSEs of the flow field predictions at the baseline case, by using the pre-determined viscosity.

[2] X. Tong, X. Zhao, Power generation control of a monopile hydrostatic wind turbine using an $\mathcal{H}_\infty$ loop-shaping torque controller and an LPV pitch controller, IEEE Transactions on Control Systems Technology 26 (6) (2018) 2165–2172.

[3] W. P. Mahoney, K. Parks, G. Wiener, Y. Liu, W. L. Myers, J. Sun, et al., A wind power forecasting system to optimize grid integration, IEEE Transactions on Sustainable Energy 3 (4) (2012) 670–682.

[4] S. Lin, X. Zhao, X. Tong, Feasibility studies of a converter-free grid-connected offshore hydrostatic wind turbine, IEEE Transactions on Sustainable Energy 11 (4) (2020) 2494–2503.

[5] Z. Shu, Q. Li, Y. He, P. Chan, Observations of offshore wind characteristics by doppler-lidar for wind energy applications, Applied Energy 169 (2016) 150–163.

[6] X.-Y. Tang, S. Zhao, B. Fan, J. Peinke, B. Stoevesandt, Micro-scale wind resource assessment in complex terrain based on cfd coupled measurement from multiple masts, Applied Energy 238 (2019) 806–815.

[7] M. Harris, M. Hand, A. Wright, Lidar for turbine control, National Renewable Energy Laboratory, Golden, CO, Report No. NREL/TP-500-39154 (2006).

[8] E. Simley, L. Pao, N. Kelley, B. Jonkman, R. Frehlich, Lidar wind speed measurements of evolving wind fields, in: 50th AIAA Aerospace Sciences Meeting including the New Horizons Forum and Aerospace Exposition, 2012, p. 656.

[9] E. Simley, L. Pao, Reducing lidar wind speed measurement error with optimal filtering, in: 2013 American Control Conference, IEEE, 2013, pp. 621–627.

[10] Z. Peng, S. Peng, L. Fu, B. Lu, J. Tang, K. Wang, et al., A novel deep learning ensemble model with data denoising for short-term wind speed forecasting, Energy Conversion and Management 207 (2020) 112524.

[11] J. Duan, H. Zuo, Y. Bai, J. Duan, M. Chang, B. Chen, Short-term wind speed forecasting using recurrent neural networks with error correction, Energy (2020) 119397.

[12] Y. Liu, H. Qin, Z. Zhang, S. Pei, Z. Jiang, Z. Feng, et al., Probabilistic spatiotemporal wind speed forecasting based on a variational bayesian deep learning model, Applied Energy 260 (2020) 114259.

[13] B. Yan, Q. Li, Coupled on-site measurement/cfd based approach for high-resolution wind resource assessment over complex terrains, Energy Conversion and Management 117 (2016) 351–366.

[14] X. Yang, C. Milliren, M. Kistner, C. Hogg, J. Marr, L. Shen, et al., High-fidelity simulations and field measurements for characterizing wind fields in a utility-scale wind farm, Applied Energy 281 (2021) 116115.

[15] P. Towers, B. L. Jones, Real-time wind field reconstruction from lidar measurements using a dynamic wind model and state estimation, Wind Energy 19 (1) (2016) 133–150.

[16] J. Mercieca, P. Aram, B. L. Jones, V. Kadirkamanathan, A spatiotemporal estimation framework for real-world lidar wind speed measurements, IEEE Transactions on Control Systems Technology 28 (4) (2020) 1595–1602.

[17] S. Sun, S. Liu, J. Liu, H. I. Schlaberg, Wind field reconstruction using inverse process with optimal sensor placement, IEEE Transactions on Sustainable Energy 10 (3) (2019) 1290–1299.

[18] S. Sun, S. Liu, M. Chen, H. Guo, An optimized sensing arrangement in wind field reconstruction using cfd and pod, IEEE Transactions on Sustainable Energy 11 (4) (2020) 2449–2456.

[19] J. Zhang, X. Zhao, Spatiotemporal wind field prediction based on physics-

[1] A. Scholbrock, P. Fleming, D. Schlipf, A. Wright, K. Johnson, N. Wang, Lidar-enhanced wind turbine control: Past, present, and future, in: 2016 American Control Conference (ACC), IEEE, 2016, pp. 1399–1406.

Algorithm 1 The training and prediction procedure of the proposed method

---

1: % The training of the deep learning model
2: Load all the LIDAR measurement data of size N_μ, i.e. $\{[t_i^\mu, x_i^\mu, y_i^\mu, z_i^\mu, \theta_i^\mu, \phi_i^\mu, u_i^\mu], 1 \le i \le N_\mu\}$.
3: Initialize $1/Re$ with the Re number calculated based on air viscosity.
4: Set the batch size of the spatiotemporal coordinates for enforcing the NS constraints N_{ns}.
5: Set the total number of training iterations N_{tot}.
6: Set the learning rate lr.
7: $j \leftarrow 1$.
8: **while** $j \le N_{tot}$ **do**
9:     Generate the spatiotemporal coordinates of size N_{ns} corresponding to the 3-D domain in front of the wind turbine, i.e. $\{[t_i^{ns}, x_i^{ns}, y_i^{ns}, z_i^{ns}], 1 \le i \le N_{ns}\}$.
10:     Train the deep learning model to minimize the loss $L(W, 1/Re)$ with the learning rate of lr, by feeding $\{[t_i^\mu, x_i^\mu, y_i^\mu, z_i^\mu, \theta_i^\mu, \phi_i^\mu, u_i^\mu], 1 \le i \le N_\mu\}$ and $\{[t_i^{ns}, x_i^{ns}, y_i^{ns}, z_i^{ns}], 1 \le i \le N_{ns}\}$ to the neural network structure. The training variables are $[W, 1/Re]$.
11:     $j \leftarrow j + 1$.
12: **end while**
13: The estimation of the effective viscosity is obtained based on the converged value of $1/Re$.

14: % The prediction of the 3-D spatiotempoal wind field
15: Specify a time coordinate t_{test}.
16: Specify a point cloud of size N_{test} (i.e. $\{[x_k, y_k, z_k], 1 \le k \le N_{test}\}$) corresponding to the 3D flow domain in front of the wind turbine.
17: **for** k in [1,2,...,N_{test}] **do**
18:     Propagate $[x_k, y_k, z_k, t_{test}]$ through the Base-NN to predict u, v, and w at the location $[x_k, y_k, z_k]$ at time t_{test}.
19: **end for**
20: The 3-D wind velocity field (including the components in the x, y, and z directions) in front of the wind turbine at time t_{test} is obtained by combining the predictions at all the locations in the point cloud.

---

informed deep learning and lidar measurements, Applied Energy 288 (2021) 116641.

[20] M. Raissi, P. Perdikaris, G. E. Karniadakis, Physics-informed neural networks: A deep learning framework for solving forward and inverse problems involving nonlinear partial differential equations, Journal of Computational Physics 378 (2019) 686–707.

[21] J. Li, X. Wang, X. B. Yu, Use of spatio-temporal calibrated wind shear model to improve accuracy of wind resource assessment, Applied energy 213 (2018) 469–485.

[22] D.-Y. Kim, Y.-H. Kim, B.-S. Kim, Changes in wind turbine power characteristics and annual energy production due to atmospheric stability, turbulence intensity, and wind shear, Energy 214 (2021) 119051.

[23] M. Churchfield, S. Lee, Nwtc design codes-sowfa, URL: http://wind.nrel.gov/designcodes/simulators/SOWFA (2012).

[24] M. J. Churchfield, S. Lee, J. Michalakes, P. J. Moriarty, A numerical study of the effects of atmospheric and wake turbulence on wind turbine dynamics, Journal of turbulence (13) (2012) N14.

[25] P. Fleming, P. M. Gebraad, S. Lee, J.-W. van Wingerden, K. Johnson, M. Churchfield, et al., Simulation comparison of wake mitigation control strategies for a two-turbine case, Wind Energy 18 (12) (2015) 2135–2143.

[26] H. Dong, J. Zhang, X. Zhao, Intelligent wind farm control via deep reinforcement learning and high-fidelity simulations, Applied Energy 292 (2021) 116928.

[27] P. Doubrawa, M. J. Churchfield, M. Godvik, S. Sirnivas, Load response of a floating wind turbine to turbulent atmospheric flow, Applied Energy 242 (2019) 1588–1599.

[28] G. I. Taylor, The spectrum of turbulence, Proceedings of the Royal Society of London. Series A-Mathematical and Physical Sciences 164 (919) (1938) 476–490.

[29] T. K. Barlas, G. A. van Kuik, Review of state of the art in smart rotor control research for wind turbines, Progress in Aerospace Sciences 46 (1) (2010) 1–27.

[30] M. Raissi, Z. Wang, M. S. Triantafyllou, G. E. Karniadakis, Deep learning of vortex-induced vibrations, Journal of Fluid Mechanics 861 (2019)

119–137.

[31] M. Raissi, A. Yazdani, G. E. Karniadakis, Hidden fluid mechanics: Learning velocity and pressure fields from flow visualizations, Science 367 (6481) (2020) 1026–1030.

[32] S. Cai, H. Li, F. Zheng, F. Kong, M. Dao, G. E. Karniadakis, et al., Artificial intelligence velocimetry and microaneurysm-on-a-chip for three-dimensional analysis of blood flow in physiology and disease, Proceedings of the National Academy of Sciences 118 (13) (2021).

[33] A. G. Baydin, B. A. Pearlmutter, A. A. Radul, J. M. Siskind, Automatic differentiation in machine learning: a survey, The Journal of Machine Learning Research 18 (1) (2017) 5595–5637.

[34] D. P. Kingma, J. Ba, Adam: A method for stochastic optimization, arXiv preprint arXiv:1412.6980 (2014).

[35] D. Choi, W. Shin, K. Ko, W. Rhee, Static and dynamic yaw misalignments of wind turbines and machine learning based correction methods using lidar data, IEEE Transactions on Sustainable Energy 10 (2) (2018) 971–982.

[36] J. Annoni, A. Scholbrock, M. Churchfield, P. Fleming, Evaluating tilt for wind plants, in: 2017 American Control Conference (ACC), IEEE, 2017, pp. 717–722.

[37] P. A. Fleming, A. Scholbrock, A. Jehu, S. Davoust, E. Osler, A. D. Wright, et al., Field-test results using a nacelle-mounted lidar for improving wind turbine power capture by reducing yaw misalignment, in: Journal of Physics: Conference Series, Vol. 524, IOP Publishing, 2014, p. 012002.